Spatial and temporal modulation of exciton photoluminescence properties in GaAs/AlAs dynamic quantum dots formed by surface acoustic waves

Tetsuomi Sogawa,[1,*] Haruki Sanada,[1] Hideki Gotoh,[1] Hiroshi Yamaguchi,[1] Sen Miyashita,[2] and Paulo V. Santos[3]

[1]*NTT Basic Research Laboratories, NTT Corporation, 3-1 Morinosato-Wakamiya, Atsugi, Kanagawa 243-0198, Japan*

[2]*NTT Advanced Technology Corporation, 3-1 Morinosato-Wakamiya, Atsugi, Kanagawa 243-0198, Japan*

[3]*Paul Drude Institute, Hausvogteiplatz 5-7, 10117 Berlin, Germany*

We report on the dynamic optical properties of excitons in moving dots (dynamic quantum dots, DQDs) formed by the interference of orthogonally propagating surface acoustic waves (SAWs) in GaAs/AlAs quantum wells. Spatially and time-resolved photoluminescence (PL) measurements using a synchronized excitation method clearly demonstrate the formation of two interpenetrating square arrays of DQDs, one consisting of potential dynamic dots (p-DDs) formed by the SAW piezoelectric potential and the other consisting of strain dynamic dots created by the strain-induced band-gap modulation. We found that the p-DDs induce a PL-polarization anisotropy, leading to a checkered spatial modulation pattern for the preferential PL-polarization direction. Carrier dynamics under SAW fields, which affect the effective diffusion length of excitons and the PL quenching time, is invoked to clarify the physical mechanisms underlying the PL-mapping spectra obtained by the synchronized excitation method. A theoretical analysis on the band structures and optical transition properties modified by SAWs consistently explains the experimental results.

I. INTRODUCTION

Quantum confinement of carriers in artificial semiconductor structures has contributed to fundamental scientific studies as well as to the development of electrical and optical devices.[1] In particular, basic physical properties such as the electronic band gap and the strength of excitonic transitions can be controlled in quantum-well (QW) structures by using sophisticated epitaxial growth techniques based on the static control of material composition and dimensions. Although various approaches have been demonstrated to further reduce the dimensionality of the structures to one or zero dimensions, this dimensionality reduction has normally been accompanied by deleterious effects induced by lateral interfaces and/or by fluctuations in structural dimensions. Surface acoustic waves (SAWs) provide an alternative way of introducing a dynamic one-dimensional or two-dimensional (2D) lateral modulation of the band structure of QWs while avoiding these deleterious effects.[2–11] Furthermore, the band modulation introduced by SAWs differs qualitatively from that induced by a static modulation because its time and spatial dependence allows for dynamic control of the material properties. In fact, novel dynamic properties have been reported including photoluminescence (PL) quenching due to the lateral piezoelectric field and subsequent recombination of the separated carriers after the macroscopic transport,[3,7] the polarization anisotropy of PL spectra caused by strain-induced band mixing,[6,9] and spin manipulation capability.[12–14]

In this paper, we investigate the dynamic optical properties of excitons in GaAs/AlAs moving dots (dynamic quantum dots, DQDs) (Ref. 8) formed by the interference of SAW beams. The SAWs induce a strain as well as a piezoelectric modulation of the materials properties. Spatially resolved PL measurement using a synchronized excitation method clearly demonstrates that the 2D SAW interference forms two interpenetrating square arrays of DQDs: one consisting of potential dynamic dots (p-DDs) created by the modulation of the piezoelectric potential (Φ_{SAW}) and the other consisting of strain dynamic dots (s-DDs) formed by the strain-induced band-gap modulation.[8] It is shown that only p-DDs introduce a PL-polarization anisotropy, which results in a checkered-pattern modulation of the preferential PL-polarization direction. Carrier dynamics including the effective diffusion length of excitons as well as the PL quenching under SAW fields have been investigated to clarify the details of the PL-mapping spectra obtained by the synchronized excitation method. A theoretical analysis on the band structures and optical transition properties modified by SAWs provides a consistent explanation for the experimental results.

In Sec. II, we describe the sample structures and experimental techniques that we used to measure the PL dynamics under acoustic excitation. We present the experimental results in Sec. III, where we report both the spatial (Sec. III A) and time-dependent (Sec. III B) PL-modulation induced by the 2D SAWs. Then, we discuss the carrier dynamics in DQDs (Sec. IV A) and theoretically analyze the SAW-induced band modulation to explain the experimental results (Sec. IV B). Our conclusions are summarized in Sec. V.

II. EXPERIMENTAL DETAILS

The investigations were performed on a sample containing eight GaAs single QWs with various well thicknesses L_z (=6.3, 7.1, 8.3, 9.9, 12.2, 15.2, 19.8, and 83 nm) (Ref. 15) separated by seven-period AlAs(2.0 nm)/GaAs(2.0 nm) short-period superlattice barriers grown on (001) GaAs by molecular-beam epitaxy. The QWs are located between 100 and 400 nm from the surface, on which interdigital transducers have been deposited to generate SAWs propagating along the [110] and [1−10] directions. The interference of these acoustic beams leads to the formation of DQDs moving
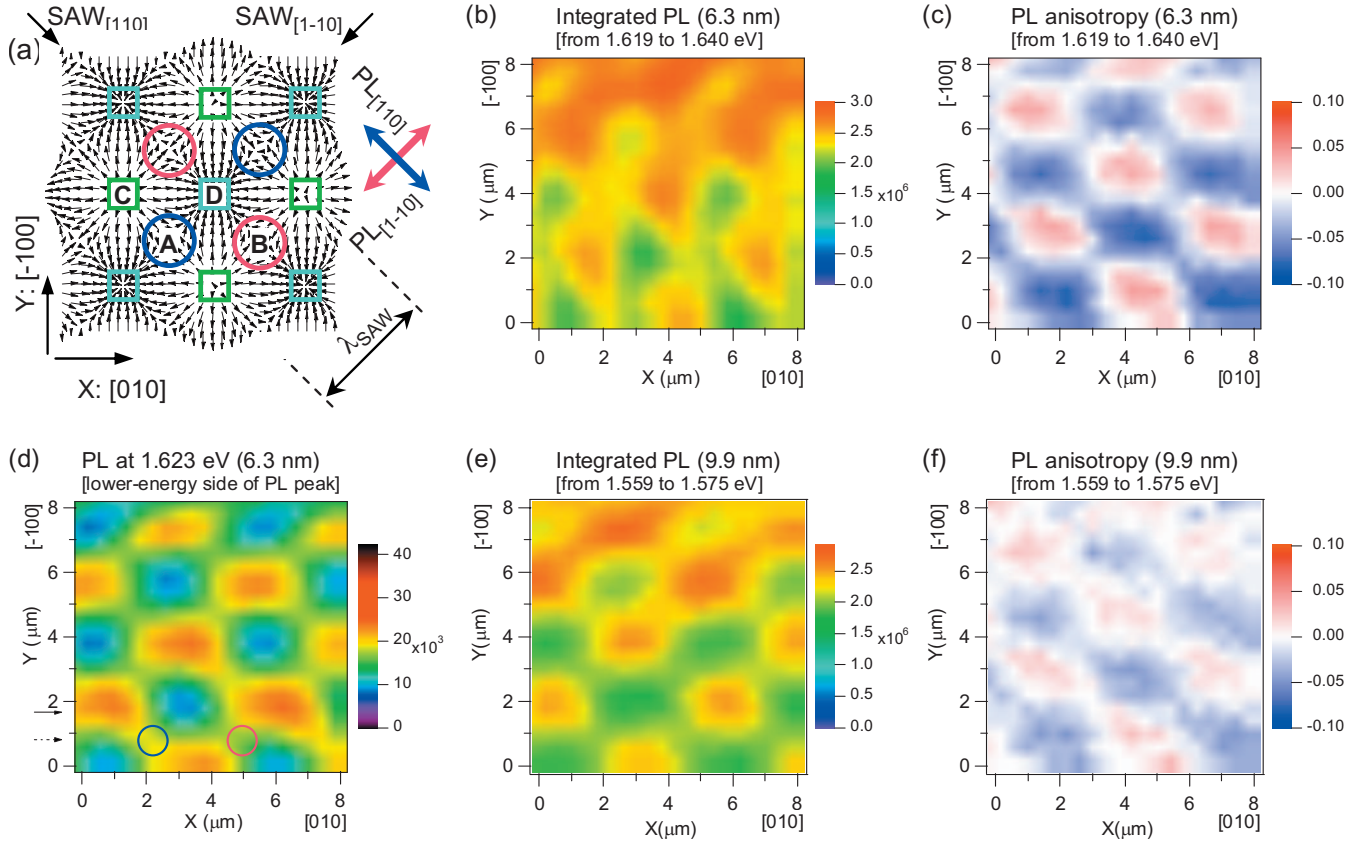
FIG. 1. (Color) (a) Schematic illustration of the in-plane components of the particle displacement field with electron-attractive (hole-attractive) p-DDs denoted by red (blue) circles, and tensile (compressive) s-DDs denoted by green (light blue) squares. (b) Spatial distribution of the PL intensity for the 6.3 nm QW measured by the CCD detector and integrated from 1.619 to 1.640 eV, (c) degree of PL polarization (ρ), and (d) spatial distribution of the PL intensity recorded at a photon energy of 1.623 eV. (e) Spatial distribution of the PL intensity from the 9.9 nm QW and (f) ρ, integrated from 1.559 to 1.575 eV.

along the [100] direction, as illustrated in Fig. 1(a). As the SAW frequency is 820 MHz, the spatial modulation period (i.e., the SAW wavelength λ_{SAW}) corresponds to about 3.6 μm, as obtained from the SAW phase velocity (v_{SAW}) of 2950 m/s. Low-temperature (4 K) spatially resolved PL spectra were measured in a helium gas-flow cryostat using a confocal micro-PL setup with a spatial resolution of approximately 1 μm. Mode-locked pulses (1.5 ps, 82 MHz, 720 nm, and 15–30 μW) from a Ti-sapphire laser synchronized with the SAW frequency were used to generate carriers, i.e., one optical excitation pulse for every ten SAW periods. The PL was spectrally analyzed by a spectrometer connected to a charge-coupled-device (CCD) detector or a synchronously scanning streak camera.

Spatial modulation of the band structure, a unique feature introduced by the SAW-induced dynamic modulation, was studied using microscopic reflectance and reflectance anisotropy.[5] In the present study, we adopted a PL-mapping technique using synchronized light excitation to investigate the spatial modulation induced by SAWs.[11] If an appropriate excitation carrier density is chosen, the lateral component of the SAW piezoelectric field becomes partially screened after the arrival of the excitation pulse. Subsequently (i.e., after a few hundred ps), as the carrier density decreases and the piezoelectric field recovers, the PL becomes strongly sup-

pressed by the spatial separation of electrons and holes. As a result, most of the emission occurs within the first few hundred ps after the laser pulse and primarily reflects the band structure around the microscopic carrier-generation spot. The travel distance of the SAW fields during the 200 ps time interval after the laser pulse, which corresponds to approximately 0.6 μm, is smaller than the spatial resolution of the experimental setup. Thus, even if the CCD detects the time-integrated PL intensity, the spatial modulation can be visualized by the synchronized PL-mapping measurement, as discussed in Sec. IV A.

In the experimental configuration shown in Fig. 1(a) with the $X=[010]$ and $Y=[-100]$ axes oriented along the horizontal and vertical directions, respectively, the SAW beams travel from top right to bottom left and top left to bottom right. The DQDs move in the $-Y$ direction (i.e., toward the bottom). Spatially resolved PL measurements were carried out by scanning the sample stage along X and Y with a step of 0.4 μm. In the PL-polarization studies, we define the degree of polarization anisotropy ρ as the relative difference $\rho=(PL_{[1-10]}-PL_{[110]})/(PL_{[1-10]}+PL_{[110]})$ between the PL intensity emitted along the [1–10] ($PL_{[1-10]}$) and [110] ($PL_{[110]}$) propagation directions of the individual SAW beam. The SAW linear-power density P_l per beam (defined as the acoustic power flux per unit length along the cross section of the

SAW beam) was in the range from 70 to 100 W/m as estimated from a comparison of the observed band-gap energy shifts in the PL spectra and the theoretical values.[6]

III. RESULTS

A. Spatial PL modulation by 2D SAWs

Figures 1(b) and 1(c) show the spatial distributions of the PL intensity and ρ, respectively, for the 6.3 nm QW, obtained by integrating PL spectra measured by the CCD detector in the energy range from 1.619 to 1.640 eV. The PL-mapping data appear to be compressed along the Y direction and slightly shifted toward the $-X$ direction as the Y position increases because the drift of the setup might occur while moving the stage by a raster scan mode. Thus, only the X axis represents the actual scale of the spatial modulation while the Y axis should be calibrated by multiplying a factor of 1.3–1.4 to compensate for the distortion caused by the drift. Figure 1(b) clearly shows the formation of a square array of bright dotlike PL areas. The spatial distribution of ρ in Fig. 1(c) exhibits a checkered pattern with maxima that are slightly shifted along the Y direction with respect to the dotlike structure in Fig. 1(b). Figure 1(d) shows the PL mapping for the 6.3 nm QW recorded at a photon energy of 1.623 eV, which is located in the lower-energy side of the PL peak (centered at 1.630 eV in the absence of a SAW). Figures 1(e) and 1(f) show the spatial distributions of the PL intensity and ρ for the 9.9 nm QW integrated from 1.559 to 1.575 eV, respectively. The positions with maximum and minimum ρ in Fig. 1(f) coincide with those for the 6.3 nm QW in Fig. 1(c). On the other hand, the areas of strong integrated PL for the 9.9 nm QW appear at the maximum PL positions in Fig. 1(d). We also found that the shapes of the strong integrated PL areas change from triangular for the 6.3 nm QW [cf. Fig. 1(b)] to square for the 9.9 nm QW [cf. Fig. 1(e)].

The single SAW introduces spatial modulation of both Φ_{SAW} and band-gap energy along the QW plane. Due to the D_{4d} symmetry of the underlying GaAs crystal, the phase relationship between the two modulation depends on the SAW propagation direction,[8] i.e., a position with a maximum band-gap energy exhibits negative (positive) Φ_{SAW} for the SAW propagating along the [110] ([1–10]) direction. As a consequence, the interference of two orthogonal SAW beams leads to the formation of two interpenetrating square arrays of DQDs, as shown in Fig. 1(a), where the in-plane components of the particle displacement field are shown schematically. One of the arrays (red and blue circles) consists of p-DDs formed by the Φ_{SAW} modulation. The second array (green and light-blue squares) is composed of s-DDs, where the band gap becomes minimum or maximum due to the hydrostatic strain.[8] The strong (red) and weak (blue) PL positions in Fig. 1(d) correspond to the tensile [green squares in Fig. 1(a)] and compressive [light-blue squares in Fig. 1(a)] s-DD positions, respectively. A comparison of Figs. 1(c) and 1(d) demonstrates that the positive ρ areas are located at the saddle point of the tensile s-DDs along the [1–10] direction, denoted by a red circle in Fig. 1(d), while the negative ρ areas are situated at the saddle point of the tensile s-DDs along the [110] direction, denoted by a blue circle in Fig.

1(d). Taking into account the field distribution in Fig. 1(a), we thus conclude that the areas of the maximum (minimum) ρ coincide with the position of the positive (negative) p-DDs, as denoted by the red (blue) circles.

Figures 2(a) and 2(b) display slices of the PL-mapping spectra along the X direction recorded at $Y = 1.6$ and 0.8 μm, which are indicated by solid and dashed arrows in Fig. 1(d) and correspond to rows of s-DDs and p-DDs, respectively. The PL emission around 1.626 eV originates from the 6.3 nm QW. The spectra recorded along the row of s-DDs [Fig. 2(a)] clearly show the band-gap modulation along X caused by the SAW-induced strain. The spatial period of the modulation of 5.0–5.4 μm agrees with the lattice constant of the DQD array $\lambda_{SAW}^* (= \sqrt{2} \lambda_{SAW})$ expected from the SAW interference grating. In contrast, the band-gap modulation is reduced along the row of p-DDs [Fig. 2(b)], where the hydrostatic strain vanishes[8] if the two orthogonal SAW beams have the same amplitude. We also found that the 6.3 nm and 7.1 nm QWs exhibit a PL-intensity modulation along the p-DD row with half of the period of the spatial band-gap modulation. These intensity oscillations are attributed to the emission from positive (electron attractive) and negative (hole attractive) p-DDs, which are separated by $\lambda_{SAW}^*/2$ [cf. Fig. 1(a)]. In thick QWs ($L_z \geq 8.3$ nm), this half-period modulation of the PL intensity disappears [cf. Fig. 2(b)]. PL blue shifts at the compressive s-DDs (around $X = 3.6$ μm) are clearly observed for thin QWs ($L_z \leq 7.1$ nm) in Fig. 2(a), where the emission energies of the PL peaks observed in the absence of SAWs are indicated by arrows. In contrast, the thick QWs exhibit energy shifts only toward lower energies, i.e., the modulation in the higher-energy side becomes less pronounced. As discussed in Sec. IV A, these effects are associated with the exciton diffusion length,[16] which increases with increasing L_z.

B. Temporal PL properties modulated by 2D SAWs

To clarify the influence of the SAW fields on the temporal behavior of excitons and carriers in DQDs, we have measured time-resolved PL spectra for excitation at four different positions within a DQDs array, denoted by capitals A–D in Fig. 1(a). Carriers were generated by ps pulses at the positions estimated as the negative p-DD (A), positive p-DD (B), tensile s-DD (C), and compressive s-DD (D), by moving the sample stage according to the PL-mapping data. Figures 3(a) and 3(b) show time-resolved PL spectra for A and D, respectively, as measured by the streak camera. The SAW fields drastically change the excitonic recombination spectra from the monotonous decay in the absence of SAWs, shown in Fig. 3(c), into the rapid PL quenching as well as the oscillatory behaviors of the PL intensities and emission energies. Figure 3(d) compares the PL spectra for A–D (solid lines) and in the absence of SAWs (dashed line), where the spectra were integrated during the initial 100 ps after the excitation. The broadening of the PL linewidths compared to those without SAWs is attributed to the inhomogeneous broadening due to the strain-induced distribution of band-gap energies within the detection spot. The spectra for the positions A and B are similar while the position C (D) exhibits an enhanced PL
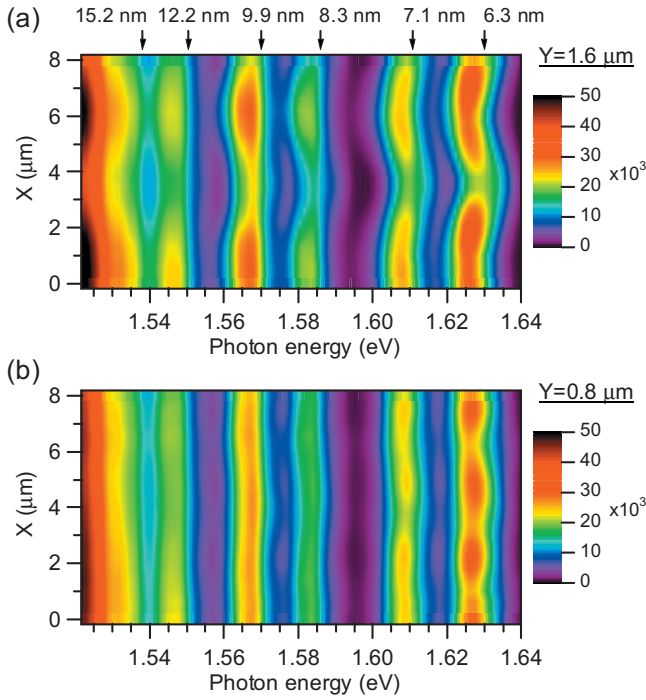
FIG. 2. (Color) Slice of the PL spectra along the *X* direction for the vertical positions of (a) *Y*=1.6 *μ*m and (b) *Y*=0.8 *μ*m.

broadening toward the lower(higher)-energy side with respect to the spectra for A and B because of the reduced (enhanced) band gap.

Figures 4(a)–4(d) represent the PL time traces for the 7.1, 8.3, 9.9, and 12.2 nm QWs (solid lines), respectively, measured at positions A–D, while the dashed lines show the corresponding PL time traces in the absence of SAWs. We found that the PL quenching becomes more significant as L_z decreases. As regards the position dependence, the positions C and D have similar decay profiles while the position A exhibits faster quenching than C and D. The position B shows the slowest decay as well as shoulder structures, which appear around *t*=600 ps. For all positions, the subsequent PL peaks appear around *t*=1200 ps, which corresponds to the next SAW cycle. If carriers are generated when the center of the p-DD arrives at the excitation (and detection) position, the *Y* component of the lateral (i.e., in the QW plane) piezoelectric field becomes maximum at *t*=300 and 900 ps. On the other hand, as shown in Fig. 1(a), the s-DDs correspond to the saddle points of the Φ_{SAW} modulation. The Φ_{SAW} modulation disappears on the moving path of the s-DDs,[8] while the *X* component of the lateral piezoelectric field varies, i.e., if carriers are generated at the center of the s-DD, the *X* component becomes maximum at *t*=300 and 900 ps. It is reported that the band-gap modulation causes a sufficiently strong effective field for excitons to move as fast as v_{SAW}.[11,17] However, the similarity of the PL time traces for the positions C (i.e., tensile strain) and D (i.e., compressive strain) in Fig. 4 suggests that the PL quenching is not caused by the sweep of excitons trapped at the tensile s-DD from the detection spot but is determined by exciton ionization caused by the strong lateral piezoelectric field (*X* component) around *t*=300 ps.
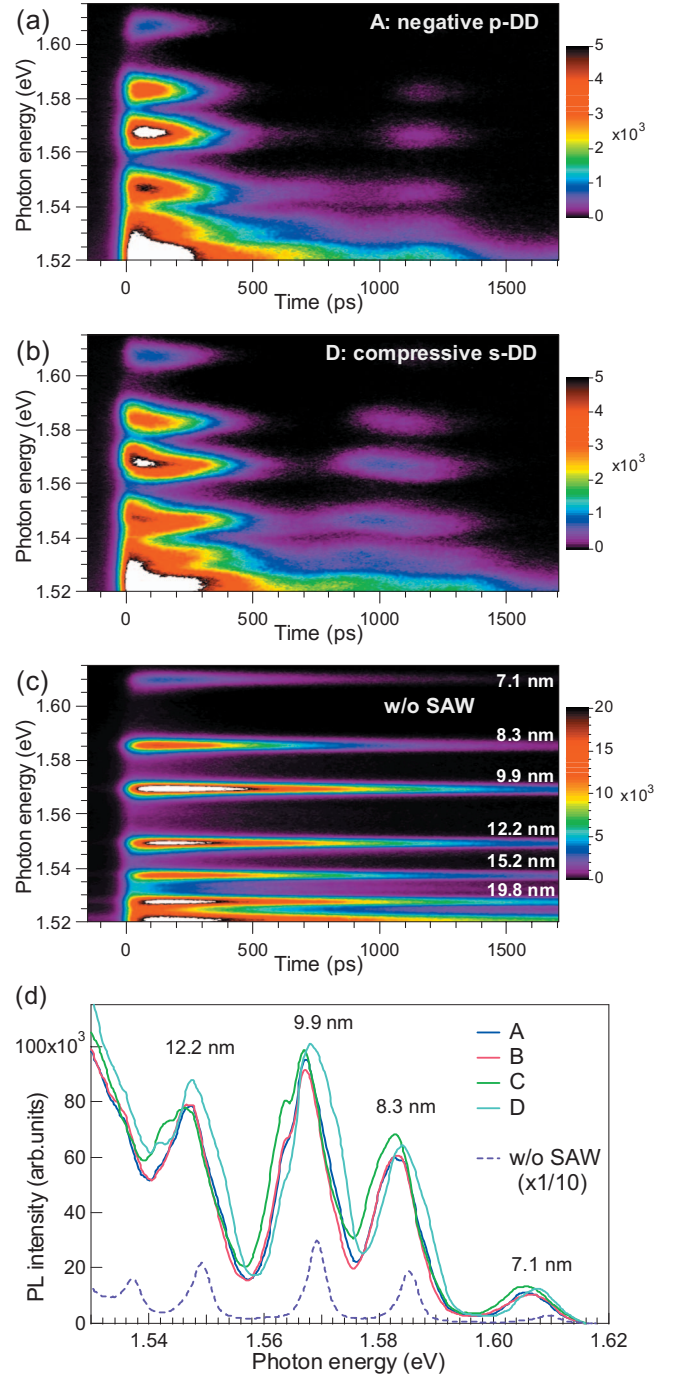

FIG. 3. (Color) [(a) and (b)] Time-resolved PL spectra measured at a negative p-DD and a compressive s-DD, denoted by A and D, respectively. (c) Time-resolved PL spectra in the absence of SAWs. (d) Time-integrated spectra during the initial 100 ps after excitation at positions A–D (solid lines) and in the absence of SAWs (dashed line)

IV. DISCUSSION

A. Carrier dynamics in DQDs

We now discuss the physical mechanisms for the PL modulation in more detail by considering the following two situations: (i) if the lateral piezoelectric field is not sufficiently strong to ionize excitons, neutral excitons will not
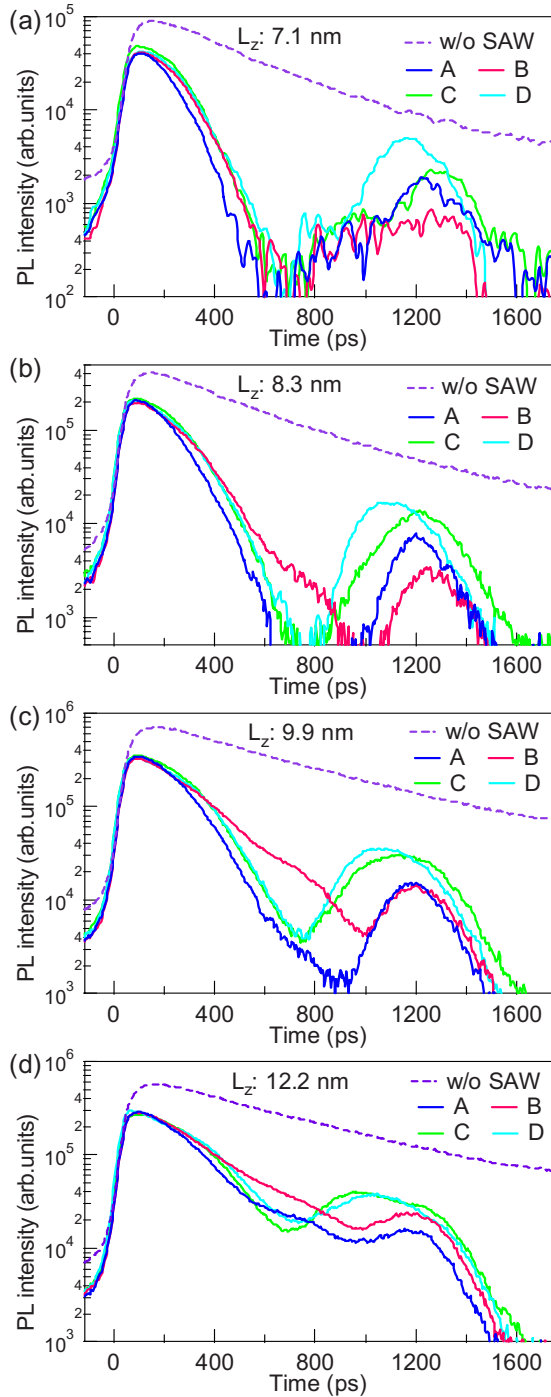
FIG. 4. (Color online) [(a)–(d)] PL time traces measured at the positions A–D (solid lines) for the 7.1, 8.3, 9.9, and 12.2 nm QWs, respectively. The dashed lines show the corresponding traces in the absence of SAWs.

feel the Φ_{SAW} modulation. The neutral excitons will expand spatially through diffusion, which is determined by the gradient of the exciton density, and also migrate toward the local minima[18] in the strain-induced band-gap modulation. If the PL decay time is long enough for the excitons to reach the local minima, the PL energies will be mainly determined by the excitonic transition energies at these minima. (ii) If the lateral piezoelectric field becomes strong enough to ion-

ize excitons, electrons and holes are attracted toward the spatially separated potential maxima and minima, which are marked in Fig. 1(a) by the red and blue circles, respectively. If some of the separated carriers spill out from the moving confinement potential via scattering or being captured at the interface potential fluctuation or defects in the barrier layers, they may still form excitons when carriers of opposite charge are brought by the next confinement potential and then emit. However, in the absence of spillover near neighboring p-DDs, no PL should be expected after the spatial separation, that is, the PL spectra become determined by the states of the excitons between the excitation and the ionization. Since the carrier density is sufficiently high to partially screen the piezoelectric field under the experimental conditions, process (i) dominates the PL emission immediately after the excitation. Then, with the decrease in carrier density, process (ii) eventually overcomes (i). The transition between (i) and (ii) depends on the excitation carrier density, P_l, L_z, and the position of the light spot relative to the DQDs. Moreover, we have to take into account the spillover effects to explain the origin of the subsequent PL peaks.

In general, the PL rise time in the absence of SAWs is determined by the relaxation time of photoexcited large-K excitons into $K=0$ excitons through acoustic phonon scattering,[19] where K is the momentum of the exciton's center-of-mass motion. Under the influence of the SAW fields, when the exciton ionization rate exceeds that of the formation of $K=0$ excitons, PL quenching starts, resulting in a reduced PL intensity compared to that in the absence of SAWs. Figure 4 shows that the PL rising profiles for DQDs, where no clear difference is observed between the four characteristic positions (A–D), overlap these obtained in the absence of SAWs during the initial 50–100 ps. Thus, the exciton relaxation process does not seem to be changed significantly by the SAW fields on this time scale. For a quantitative discussion on the spatial broadening of the excitons, we consider the effective diffusion length (L_{eff}) of excitons under the SAW fields.[20] The exciton diffusivity D_{ex} in the absence of acoustic excitation was determined from time-resolved spatial PL profiles excited by a microscopic spot. D_{ex} is given by the ratio between the square of the spatial width of the PL-intensity profile and the elapsed time after the ps-pulse excitation.[21] In Fig. 5(a), we plot D_{ex} values measured in a separate experiment (not shown here) at 4 K for each QW (solid squares) as a function of L_z, where the axis on the right corresponds to D_{ex}. We define the PL quench time (T_{quench}) as the time required for the PL intensity to be reduced to $1/e$ of the maximum PL after carrier generation. The values of T_{quench} for DQDs (open circles), which are averaged for A–D, and those obtained in the absence of SAWs (solid circles) are plotted in Fig. 5(a), where the maximum and minimum values obtained from A–D are represented by error bars. T_{quench} for DQDs increases with L_z from 290 to 460 ps while it increases from 550 to 950 ps in the absence of SAWs. Since L_{eff} is given as $L_{eff}=\sqrt{D_{ex}\cdot T_{quench}}$, the L_{eff} values for the averaged T_{quench} and in the absence of SAWs are plotted in Fig. 5(b) by open circles and solid ones, respectively, where the maximum and minimum values obtained from A–D are represented by error bars. L_{eff} increases with L_z from approximately 1.0 μm for the 7.1 nm QW to
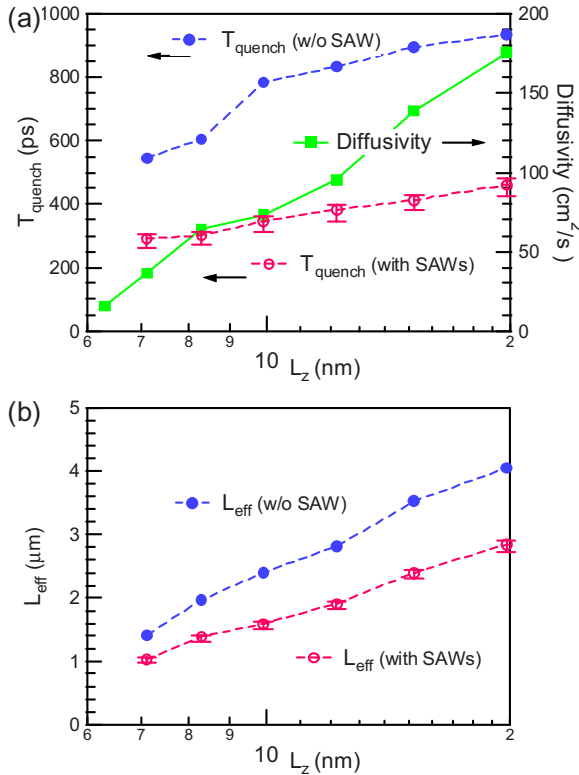
FIG. 5. (Color online) (a) Experimentally obtained values for the exciton diffusivity, D_{ex} (cm^2/s), (solid squares), and PL quench time, T_{quench} (ps), averaged for A–D (open circles) and those without SAWs (solid circles) are plotted as a function of L_z. The maximum and minimum values for the four positions are represented by error bars. (b) The estimated values of the effective diffusion length L_{eff} (μm) for the averaged T_{quench} (open circles) and without SAWs (solid circles) as a function of L_z.

2.8 μm for the 19.8 nm QW under the SAW fields, while it increases from 1.4 to 4.1 μm in the absence of SAWs. Although we could not precisely evaluate T_{quench} for the 6.3 nm QW because of limitations of the experimental setup, its L_{eff} is assumed to be less than 1 μm by considering the L_z dependences of D_{ex} and T_{quench} in Fig. 5(a).

PL-mapping spectra obtained by the synchronized excitation method clearly visualize the spatial modulation of the PL intensity and transition energies (cf., Figs. 1 and 2) at a certain moment caused by the moving SAWs. As a slow CCD detector is adopted in this measurement, the window time of the detection is roughly given as T_{quench}. To understand the physical mechanism underlying the PL-mapping spectra, we have to consider the carrier motion during T_{quench}. The areas of strong integrated PL for the 9.9 nm QW in Fig. 1(e) coincide with the tensile s-DDs, where the band gap is reduced. They correspond to the bright PL areas detected in the lower-energy side of the PL peak, as shown in Fig. 1(d). This is because the local exciton migration into the nearest tensile s-DDs dominates the emission sites due to the sufficiently long L_{eff}. In contrast, as shown in Fig. 1(b), the strong integrated PL areas for the 6.3 nm QW shift from the positions of the tensile s-DDs toward $+X$ by $\lambda_{SAW}^*/4$ (=1.25–1.35 μm). These positions correspond to the boundaries between negative p-DDs and the subsequent positive p-DDs on the moving p-DD path. To understand the findings, we should consider the asymmetry in mobilities for electrons and holes.[7] Electrons quickly follow the potential modulation due to the high electron mobility, resulting in a narrow distribution within the potential trap. In contrast, because of the relatively low hole mobility, some of the holes do not follow the changes in the potential and thus remain near the excitation spot. When carriers are generated after the positive p-DD has passed, electrons are attracted to the preceding positive p-DD, leading to the reduced PL intensity detected at the excitation position. On the other hand, when the carriers are generated after the negative p-DD, electrons are drawn toward the next-coming positive p-DD and then return to the excitation position later. Thus, the strong integrated PL areas should be located between the preceding negative p-DDs and the subsequent positive ones, which is consistent with the experimental results obtained for the 6.3 nm QW.

In Fig. 2(a), which shows the PL modulation along the row of s-DDs, the thick QWs ($L_z \geq 8.3$ nm) have their PL maximum located around $X = 0.8$ and 6.2 μm, which correspond to the positions of the tensile s-DDs. In the thin QWs ($L_z \leq 7.1$ nm), the maximum PL positions shift from the tensile s-DDs [cf. Fig. 2(a)] and the clear PL modulation appears along the row of p-DDs [cf. Fig. 2(b)]. These bright PL positions correspond to the front and rear tails of the strong integrated PL areas in Fig. 1(b). Since L_{eff} for the thick QWs exceeds the separation between the paths of the s-DDs and p-DDs (=$\lambda_{SAW}^*/4$ of 1.25–1.35 μm), most of the excitons can reach the adjacent tensile s-DDs before emission. Thus, the strongest PL positions for the thick QWs should coincide with the tensile s-DDs. On the other hand, in the 6.3 nm QW, L_{eff} (≤ 1.0 μm) is smaller than the separation. As shown in Fig. 1(b), the triangular shape of the bright PL areas is attributed to the emission from excitons that did not reach the tensile s-DDs located on the $-X$ side of the bright PL areas. It should be mentioned that the dominant PL sites depend on the experimental conditions because T_{quench} and thus L_{eff} increase as the carrier density increases due to the enhanced screening effects.

There remains a question as to why subsequent PL peaks appear around $t = 900–1000$ ps irrespective of the existence of the strong lateral piezoelectric field when carriers are generated in s-DDs, i.e., at the positions C and D, as observed in Figs. 3 and 4. Figure 3(b) shows that the PL emission energies do not increase when the second compressive s-DD reaches the detection position (at $t = 1200$ ps), suggesting that no emission is observed at the compressive s-DDs because of the rapid exciton migration toward lower-energy areas except for the initial approximately 100 ps after the excitation. When carriers are generated at the center of the s-DD, it is assumed that most of electrons (part of holes) are captured by the positive (negative) p-DD at $t = 300$ ps, which is shifted by $\pm\lambda_{SAW}^*/4$ along X from the path of the s-DDs. Then, if the electrons (holes) happen to drop out from the positive (negative) p-DD, they are attracted toward the subsequent positive (negative) p-DD, which is shifted by $\pm\lambda_{SAW}^*/2$ along X from the path of the formerly trapped p-DDs. Thus, electrons and holes, which diagonally cross the path of the s-DDs, might meet opposite carriers and form excitons near the path of the s-DDs, resulting in subsequent
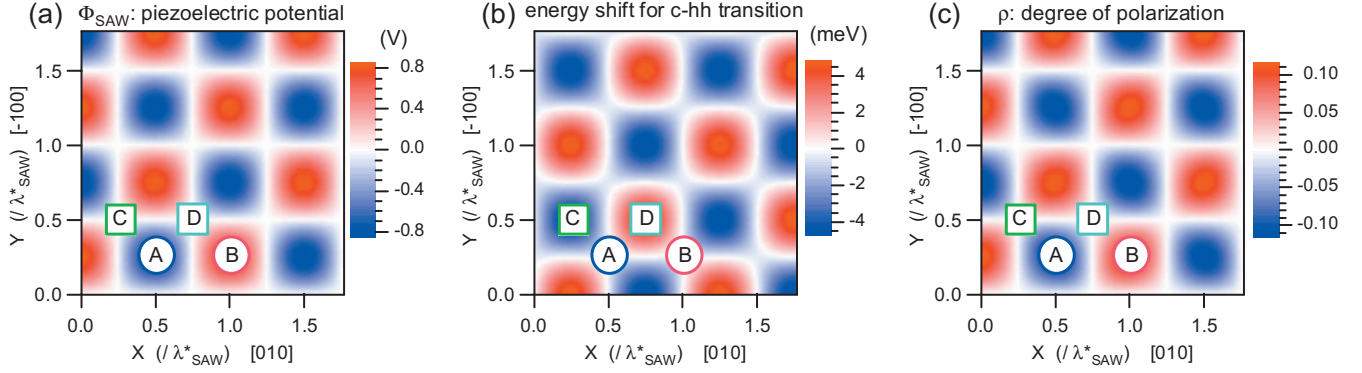
FIG. 6. (Color) Calculated spatial modulation of (a) piezoelectric potential (Φ_{SAW}), (b) transition energy shift between conduction band and heavy-hole band (c-hh), and (c) polarization anisotropy (ρ) for the c-hh transition, respectively, where the scale along the [0–10] and [100] directions is normalized by $\lambda^*_{SAW}(=\sqrt{2}\lambda_{SAW})$. A–D indicate the corresponding positions for the experimental data.

PL peaks around $t=900-1000$ ps. This is a possible explanation for the increase in PL under the lateral field. As we have not yet fully understood the physical mechanism, the investigation should be continued.

B. Theoretical analysis

To analyze the experimental results on the modulation of the band structure and the transition polarization properties theoretically, we have calculated the displacement field of the Rayleigh SAW waves including the piezoelectric coupling.[22] The results were then used to determine the energy shifts of the conduction (c), heavy-hole (hh), and light-hole (lh) bands induced by the strain using the Hamiltonian from Bir and Pikus,[23] as well as the transition matrix element for interband excitations. The calculations were based on the method described in Ref. 6. Figures 6(a)–6(c) show the calculated spatial modulation of Φ_{SAW}, the strain-induced shift of the c-hh transition energy, and ρ for the c-hh transition, respectively, where A–D denote the positions corresponding to the experiment. The scales are normalized by the lattice constant of the DQD array λ^*_{SAW}. The calculations were performed for a 6.3 nm QW, which is located 175 nm below the surface, with a SAW frequency of 800 MHz and a P_l of 100 W/m per SAW beam. For the depth of the QW and the SAW frequency used in the calculations, the band modulation is of type-II,[17] where the energy shift of the conduction band is four times that of the hh band. In Fig. 6(b), the reduced transition energy areas (blue regions) correspond to the tensile s-DDs. The positive Φ_{SAW} areas in Fig. 6(a), i.e., positive p-DDs, are located at the saddle point of the tensile s-DDs along the [1–10] direction. The polarization anisotropy is associated with the uniaxial strain profile in the p-DDs. While the hydrostatic strain vanishes, the material is subjected to a compressive (tensile) strain oriented along the [1–10] direction in the positive (negative) p-DDs. Figure 6(c) shows that areas of positive anisotropy (i.e., with stronger emission along the [1–10] direction) coincide with the positive p-DDs in Fig. 6(a). The calculated results for the spatial distribution of the anisotropy are, therefore, in good agreement with the experimental findings in Fig. 1.

A comparison between Figs. 1(c) and 6(c) shows that the measured ρ is smaller than the calculated values. In the syn-

chronized excitation method using a CCD, the observed ρ corresponds to the time-averaged ρ value during T_{quench}. Thus, it becomes smaller than the theoretical maximum value at the center of the positive p-DD. In Figs. 1(c) and 1(f), the 9.9 nm QW exhibits a smaller ρ than the 6.3 nm QW. Under the same SAW fields, thick QWs generally have a larger ρ than thin ones because the hh-lh mixing effect is enhanced due to the reduced energy separation between the hh and lh states. Although the depths and thus the strain fields differ slightly for the two QWs, the observed L_z dependence of ρ is mainly attributed to the differences in T_{quench}. In fact, in our time-resolved measurement of the PL anisotropy (not shown here), we observed that the various DQDs with different L_z exhibit similar ρ values just after the excitation. For detailed discussions on the L_z dependence of the PL anisotropy, it should be taken into account that the strain fields and, thus, the modulation of the band structures depend significantly on the depth from the surface.[17]

We briefly discuss the quantum confinement effect by the SAW-induced lateral potential modulation. For energies less than the amplitude of the piezoelectric potential Θ_{SAW} for each SAW, the 2D sinusoidal potential modulation can be approximately represented by an isotropic 2D harmonic potential. The eigenstates in this potential consist of a series of discrete states of energy relative to the bottom of the conduction band given by $n\frac{h}{\lambda_{SAW}}\sqrt{\frac{\Theta_{SAW}}{m^*}}$ ($n=1,2,\ldots$), where h is Planck's constant and m^* is the electron effective mass. A similar expression applies for the valence-band states. This formula indicates that the quantum shifts increase by reducing λ_{SAW} and increasing Θ_{SAW}, which is proportional to the square root of P_l. The quantized energy is estimated to be 1.2 meV for dynamic dots formed in a QW 175 nm below the surface by the interference of two SAW beams, each with frequency and power of 800 MHz and 100 W/m, respectively, which are the same parameters used in the calculation of Fig. 6. Although larger than the thermal energy at 4 K, the expected shift in the PL energy are difficult to detect due to the relatively large inhomogeneous PL broadening as well as to the type-II character of the modulation. A further increase in the SAW frequency (up to several GHz) and amplitude should lead to the direct observation of the quantum confinement effect. Here, we neglect the quantum confinement by

the strain-induced modulation of the band structure because the energy shift due to the strain effect is roughly two orders of magnitude smaller than that caused by the piezoelectric effect, as shown in Fig. 6. On the other hand, the strain-induced quantum confinement was successfully demonstrated by using a narrow static stressor on the surface of GaAs/AlGaAs QW,[24] where the energy shift of the conduction band induced by the hydrostatic strain is three times as large as that of this calculation and the lateral confinement gradient is steeper. If SAW operation at a higher frequency and stronger power density is achieved, the strain effects are expected to become more significant in both the quantum confinement effect and exciton trapping, which might strongly affect the optical properties.

V. CONCLUSIONS

We have investigated the dynamic optical properties of excitons in GaAs/AlAs moving dots formed by the interference of orthogonally propagating SAW beams. Spatially resolved PL measurement using a synchronized excitation method clearly demonstrates that the interference forms two interpenetrating square arrays of DQDs: one consisting of p-DDs created by the Φ_{SAW} modulation and the other consistingf of s-DDs formed by the strain-induced band-gap modulation. It is also shown that the p-DDs introduce a dynamic PL-polarization anisotropy in the form of a checkered spatial pattern. The changes in the diffusion lengths of excitons and the PL decay time under the SAW modulation were measured to clarify the physical mechanism underlying the PL-mapping spectra obtained by the synchronized excitation method. In thick QWs ($L_z \geq 8.3$ nm), the enhanced exciton migration into adjacent tensile s-DDs dominates the emission sites. In contrast, in thin QWs ($L_z \leq 7.1$ nm), the emission process occurs predominantly near the boundaries between the preceding negative p-DDs and the subsequent positive p-DD along the moving path of the p-DDs. These changes in the dominant PL areas are explained by comparing the L_z-dependent L_{eff} with the separation between the p-DDs and s-DDs. A theoretical analysis on the band structures and optical transition properties modified by the 2D SAWs consistently explains the experimental results.

*sogawa.tetsuomi@lab.ntt.co.jp

[1] C. Weisbuch and B. Vinter, *Quantum Semiconductor Structures, Fundamentals and Applications* (Academic, San Diego, CA, 1991).

[2] J. M. Shilton, V. I. Talyanskii, M. Pepper, D. A. Ritchie, J. E. F. Frost, C. J. B. Ford, C. G. Smith, and G. A. C. Jones, J. Phys.: Condens. Matter **8**, L531 (1996).

[3] C. Rocke, S. Zimmermann, A. Wixforth, J. P. Kotthaus, G. Böhm, and G. Weimann, Phys. Rev. Lett. **78**, 4099 (1997).

[4] P. V. Santos, M. Ramsteiner, and F. Jungnickel, Appl. Phys. Lett. **72**, 2099 (1998).

[5] P. V. Santos, Appl. Phys. Lett. **74**, 4002 (1999).

[6] T. Sogawa, P. V. Santos, S. K. Zhang, S. Eshlaghi, A. D. Wieck, and K. H. Ploog, Phys. Rev. B **63**, 121307(R) (2001).

[7] F. Alsina, P. V. Santos, R. Hey, A. García-Cristóbal, and A. Cantarero, Phys. Rev. B **64**, 041304(R) (2001).

[8] F. Alsina, J. A. H. Stotz, R. Hey, and P. V. Santos, Solid State Commun. **129**, 453 (2004).

[9] P. V. Santos, F. Alsina, J. A. H. Stotz, R. Hey, S. Eshlaghi, and A. D. Wieck, Phys. Rev. B **69**, 155318 (2004).

[10] T. Sogawa, H. Sanada, H. Gotoh, H. Yamaguchi, S. Miyashita, and P. V. Santos, Appl. Phys. Lett. **94**, 131912 (2009).

[11] T. Sogawa, H. Gotoh, Y. Hirayama, P. V. Santos, and K. H. Ploog, Appl. Phys. Lett. **91**, 141917 (2007).

[12] T. Sogawa, P. V. Santos, S. K. Zhang, S. Eshlaghi, A. D. Wieck, and K. H. Ploog, Phys. Rev. Lett. **87**, 276601 (2001).

[13] J. A. H. Stotz, R. Hey, P. V. Santos, and K. H. Ploog, Nature Mater. **4**, 585 (2005).

[14] O. D. D. Couto, Jr., F. Iikawa, J. Rudolph, R. Hey, and P. V. Santos, Phys. Rev. Lett. **98**, 036603 (2007).

[15] As the L_z values correspond to the nominal thicknesses at the center of a 2 inch wafer, the sample used in this experiment has slightly thinner L_z values than the nominal ones.

[16] H. Hillmer, A. Forchel, R. Sauer, and C. W. Tu, Phys. Rev. B **42**, 3220 (1990).

[17] J. Rudolph, R. Hey, and P. V. Santos, Phys. Rev. Lett. **99**, 047602 (2007).

[18] M. Zachau, J. A. Kash, and W. T. Masselink, Phys. Rev. B **44**, 8403(R) (1991).

[19] T. C. Damen, J. Shah, D. Y. Oberli, D. S. Chemla, J. E. Cunningham, and J. M. Kuo, Phys. Rev. B **42**, 7434 (1990).

[20] T. Sogawa, H. Sanada, H. Gotoh, H. Yamaguchi, S. Miyashita, and P. V. Santos, Jpn. J. Appl. Phys., Part2 **46**, L758 (2007).

[21] L. M. Smith, D. R. Wake, J. P. Wolfe, D. Levi, M. V. Klein, J. Klem, T. Henderson, and H. Morkoç, Phys. Rev. B **38**, 5788 (1988).

[22] S. H. Simon, Phys. Rev. B **54**, 13878 (1996).

[23] G. L. Bir and G. E. Pikus, *Symmetry and Strain-Induced Effects in Semiconductors* (Wiley, New York, 1974).

[24] K. Kash, B. P. Van der Gaag, D. D. Mahoney, A. S. Gozdz, L. T. Florez, J. P. Harbison, and M. D. Sturge, Phys. Rev. Lett. **67**, 1326 (1991).